Shining light on the dark side of imaging: Excited state absorption enhancement of a bis-styryl BODIPY photoacoustic contrast agent

Mathieu Frenette,[a] Maryam Hatamimoslehabadi,[b] Stephanie Bellinger-Buckley,[a] Samir Laoui,[b] Jeffrey La,[b] Seema Bag,[a] Srivalleesha Mallidi,[c] Tayyaba Hasan,[c] Brett Bouma,[c] Chandra Yelleswarapu,[b]* Jonathan Rochford[a]*

[a] Department of Chemistry, University of Massachusetts Boston, 100 Morrissey Boulevard, Boston, MA 02125. [b] Department of Physics, University of Massachusetts Boston, 100 Morrissey Boulevard, Boston, MA 02125. [c] Massachusetts General Hospital, Wellman Center for Photomedicine, 50 Blossom Street, Boston, MA 02114.

Supporting Information

Materials

BODIPY [1], (MeOPh)2BODIPY [2] and CurcuminBF$_2$ [3] were prepared according to their literature procedures. Crystal violet chloride salt was purchased from Sigma Aldrich and recrystallized from an aqueous solution with NH_4PF_6.
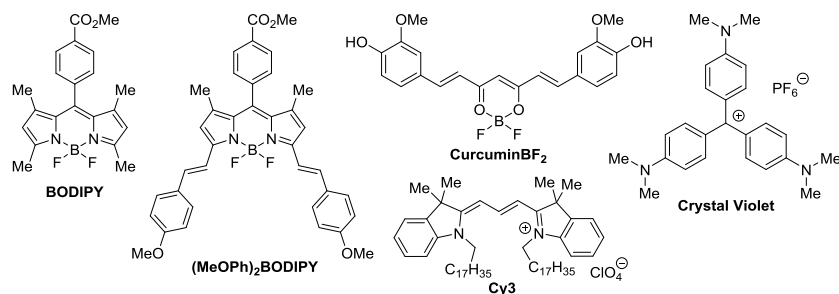
Figure S1. Molecular structures of BODIPY, (MeOPh)2BODIPY, CurcuminBF2, Cy3 and Crystal violet.

Spectral measurements and data

UV/Vis spectra were measured in spectroscopic grade acetonitrile (Sigma-Aldrich) at room temperature on an Agilent 8452 spectrophotometer using a 1 cm quartz cell. A 9:1 acetonitrile:dichloromethane mixture was required for UV/Vis (and photoacoustic) measurements of (MeOPh)2BODIPY to prevent precipitation. Steady state and time-resolved fluorescence measurements were carried out on a Photon Technology International Quantamaster 40 & 25 fluorimeter at room temperature. Fluorescence quantum yields for all samples (Φ_{fl}) were calculated by the optically dilute technique in neat acetonitrile solutions at λ_{exc} = 390 nm with fluorescein (in 0.1 M aqueous NaOH, Φ_{ref} = 0.925)[4] as the actinometer for all samples except Cy3 which was calculated at λ_{exc} = 480 nm, using with Rhodamine 6G as the actinometer (Φ_{ref} = 0.94)[5], according to eq. 1.

$$\Phi_{fl} = \left(\frac{A_{ref}}{A_s}\right)\left(\frac{I_{ref}}{I_s}\right)\left(\frac{\eta_{ref}}{\eta_s}\right)^2 \Phi_{ref} \tag{1}$$

The subscript "s" refers to the sample and the subscript "ref" to the reference sample, A is the absorbance at the excitation wavelength, I is the integrated emission area, and η is the solvent refractive index. Excitation and emission slits were both set at 2 nm. Fluorescence lifetimes ($^1\tau$) were recorded at room temperature at the emission maximum following LED excitation at 456 nm (BODIPY, CurcuminBF2) or 572 nm [(MeO2Ph)2BODIPY, Cy3]. The radiative rate constant (k_r) and non-radiative rate constant (k_{nr}) were both calculated from $^1\tau$ and Φ_{fl} by using eqs 2-5.

$$^1\tau = \frac{1}{(k_r + k_{nr})} \tag{2}$$

$$\Phi_{fl} = \frac{k_r}{(k_r + k_{nr})} \tag{3}$$

$$k_r = \frac{\Phi_{fl}}{^1\tau} \tag{4}$$

$$k_{nr} = \frac{(1 - \Phi_{fl})}{^1\tau} \tag{5}$$

Table S1. Summary of electronic absorption and fluorescence emission data for all samples in acetonitrile.

	UV/Vis (λ_{max}, nm) (ε x 10^4 M^{-1} cm^{-1})	Stokes shift (cm^{-1})	Fluorescence emission (λ_{max}, nm)	$^1\tau$ (ns)	k_r (s^{-1})	k_{nr} (s^{-1})	Φ_{fl}
BODIPY	310 (0.48), 364 (0.34), 500 (5.45)	392	510	1.98	1.55 x 10^8	3.51 x 10^8	0.306
(MeOPh)2BODIPY [a]	318 (0.93), 368 (2.70), 590 (1.54), 640 (4.34)	813	654	5.41	1.33 x 10^8	5.19 x 10^7	0.719
CurcuminBF2	499 (9.44)	3 322	591	0.72	6.67 x 10^7	1.32 x 10^9	0.048
Cy3	517 (7.56), 548 (12.59)	517	564	0.28	8.93 x 10^7	3.48 x 10^9	0.025
Crystal violet	589 (6.29)	~	~	~	~	~	0.00

[a] a 9:1 acetonitrile:dichloromethane mixture was required for UV/Vis measurements of (MeOPh)2BODIPY

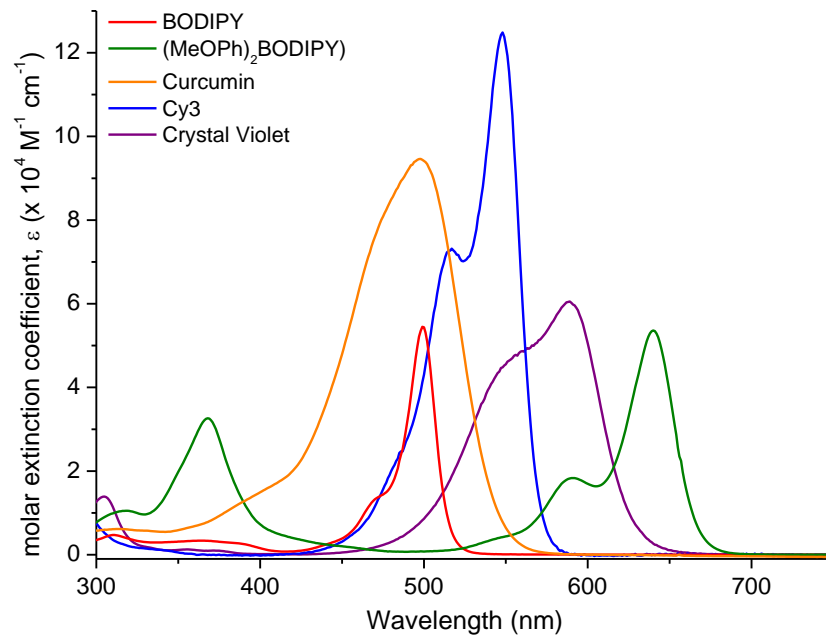**Figure S2.** Electronic absorption spectra vs. molar extinction coefficient (ε, M^{-1} cm^{-1}) of all samples recorded in acetonitrile at room temperature including crystal violet.
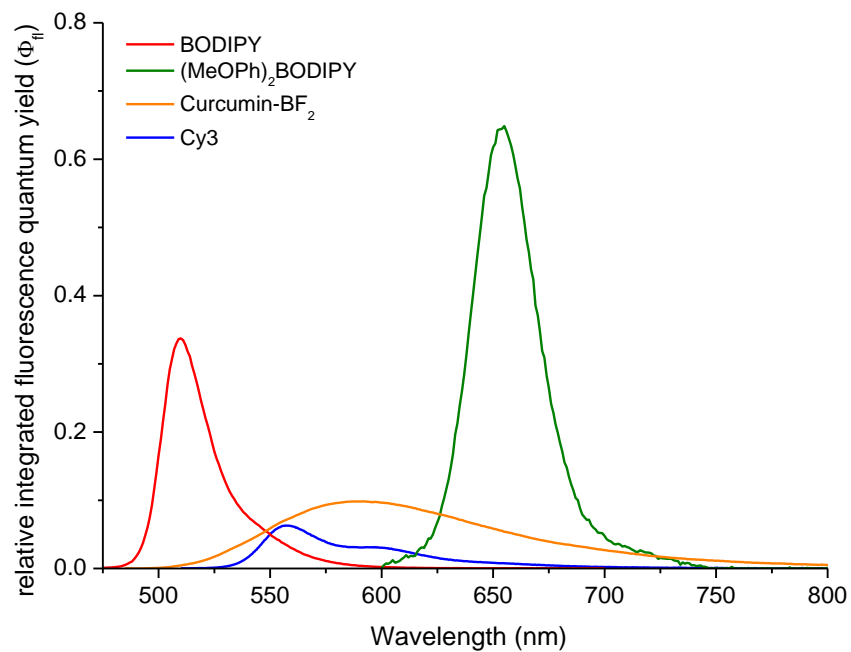

Figure S3. Fluorescence emission spectra of all samples recorded in acetonitrile. Integrated spectral areas for each sample are correlated with their respective quantum yields presented Table S1.

Computational Analysis

All calculations were carried out using density functional theory (DFT) with the B3LYP functional as implemented in the Spartan '14 program. The 6-311+g** basis set was used for all C, H, N, O and F atoms.[6, 7] Geometry optimization and subsequent single point energy calculations were carried out using a dichloromethane SM8 solvent model.[8] A vibrational frequency analysis was first carried out in the geometry optimization experiment in order to eliminate virtual transitions and confirm a global minimum energy was achieved in the chosen solvent model. Subseqently single point time-dependent density functional theory (TDDFT) was conducted to identify possible electronic transitions.[9] Trends in the UV/Vis absorption spectra can be better understood by analysis of the frontier orbitals and their respective energies. The lower electronegativity of the diaza ring system in BODIPY is responsible for destabilization of its HOMO level relative to the β-diketonate ring system in curcuminBF$_2$. The *para*-methoxyphenyl bis-styryl functionality destabilizes the HOMO level of (MeOPh)$_2$BODIPY which is responsible for its red shifted absorption maximum relative to the simple BODIPY reference.
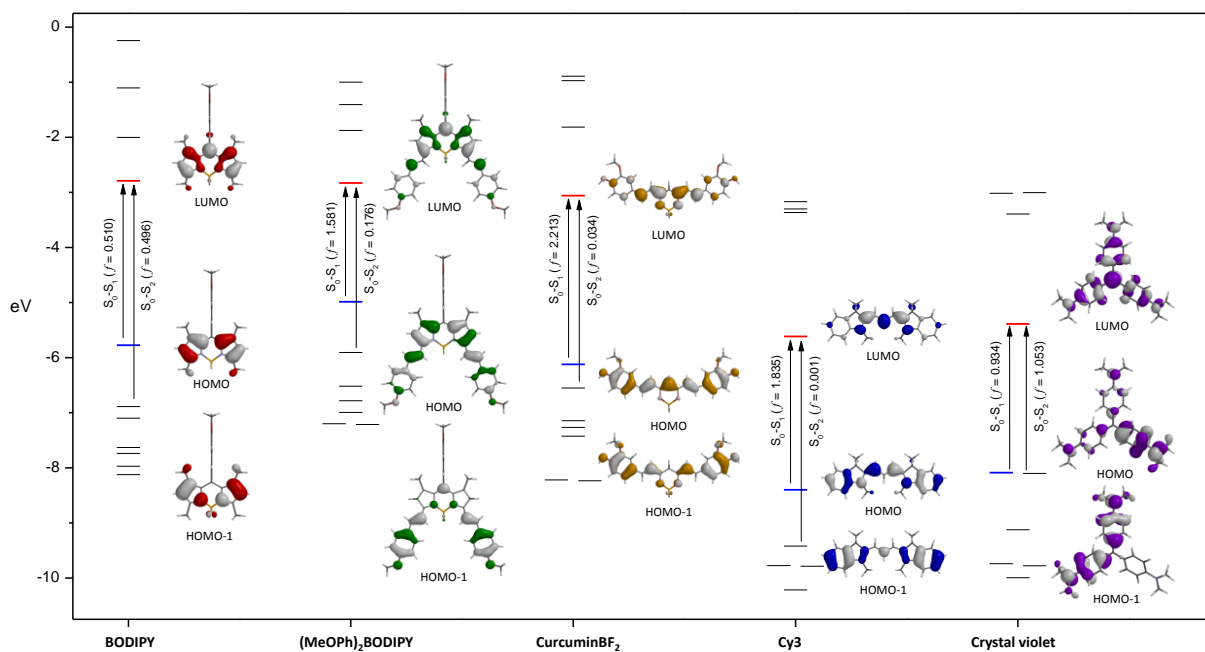

Figure S4. Molecular orbital energy diagram as calculated by density functional theory using the B3LYP functional with a 6-311+g** basis set and an acetonitrile SM8 solvent model. The HOMO, HOMO-1 and LUMO images are included as they contribute to the S$_0$→S$_1$ and S$_0$→S$_2$ electronic transitions (illustrated) for all dyes.

PAZ-scan experimental details

For PAZ-scan measurements a 2.0 mm path length quartz cell was placed at a 45^0 angle with respective to the incident laser beam (effective path length = 2.83 mm). A custom made sample cell housing unit was used wherein the quartz cell is placed and is filled with water for acoustic signal transmission. Samples were dissolved in spectroscopic grade acetonitrile having a linear absorption coefficient (α) of 345 m^{-1} at the laser excitation wavelength 532 nm (optical density = 0.3). A 9:1 acetonitrile:dichloromethane mixture was required for (MeOPh)2BODIPY alone to prevent precipitation during data collection. The output of a frequency doubled Nd:YAG laser (Continuum Minilite II, 532 nm, pulse width ~3 ns) was focused onto the sample using a 18 cm focal length lens. The sample was mounted on an automated translation stage (Thorlabs NRT 150) and moved horizontally along the Z direction through the focal point of the beam. Each Z-scan experiment took roughly 7 minutes in total. Samples were translated along the Z-axis over 15 cm in steps of 5 mm. At each position the photoacoustic and optical signals were recorded by averaging the response of 20 laser pulses (@ 10 Hz = 2 sec. duration). UV/Vis absorption spectra were recorded before and after each Z-scan experiment to ensure the stability of the sample. No degradation was observed under these experimental conditions for the series of dyes presented. Each experiment was repeated 3 times with freshly prepared sample to check for reproducibility. The beam waist (x$_0$) at focal plane was estimated to be 70 ± 5 μm. The energy incident on the sample was controlled by the combination of a half-wave plate and a linear polarizer. The incident laser energy before the focusing lens

was 65 μJ. At the focal point the sample experiences optimum pump intensity, which decreases gradually on either side of the focus as the sample is translated along the Z axis. As the fluence of incident light changes, the optical transmittance varies according to the sample's nonlinear electronic absorption properties. PA + optical and fluorescence + optical Z-scan experiments were conducted separately, both experiments having in common the optical response to allow correlation of both PA and fluorescence data collected during both Z-scan experiments. Fluorescence data was collected using an Ocean Optics fiber spectrometer USB2000 probe. The PA emission was collected using a 10 MHz, 1 inch focal length water immersion ultrasonic transducer (Olympus NDT U8517074). Importantly, the linear response of the optical detector as well as the ultrasound transducer were verified by measuring the transmittance and the corresponding generated PA response as a function of crystal violet concentration in acetonitrile (optical density from 0 to 1) at 532 nm (Figure S5). A correlation better than R2 = 0.99 was obtained for transmittance measurements when a neutral density filter of OD 1 was placed in front of the detector (Newport 818 series photodiode sensor with a 3 OD filter; data not shown) while the PA signal showed excellent linearity (Fig. S5). Crystal violet was chosen as our calibration standard due to its linear photoacoustic response with respective to laser fluence (Figure S5).
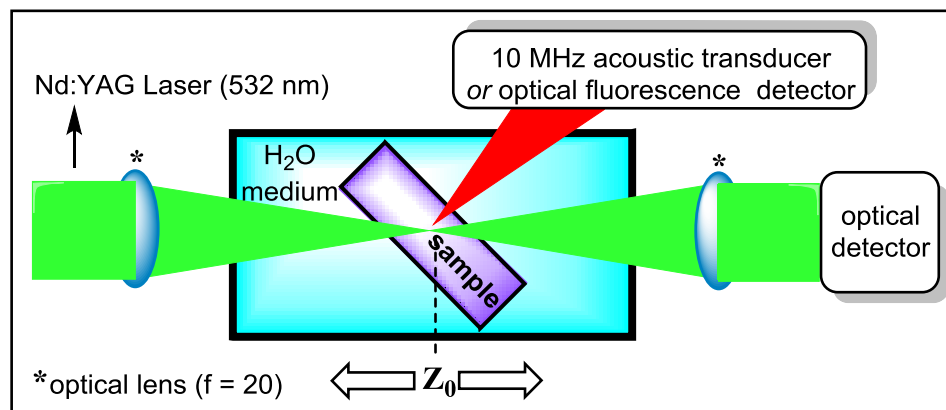
Scheme S1. Experimental setup for fluorescence and photoacoustic optical Z-Scan experiments.
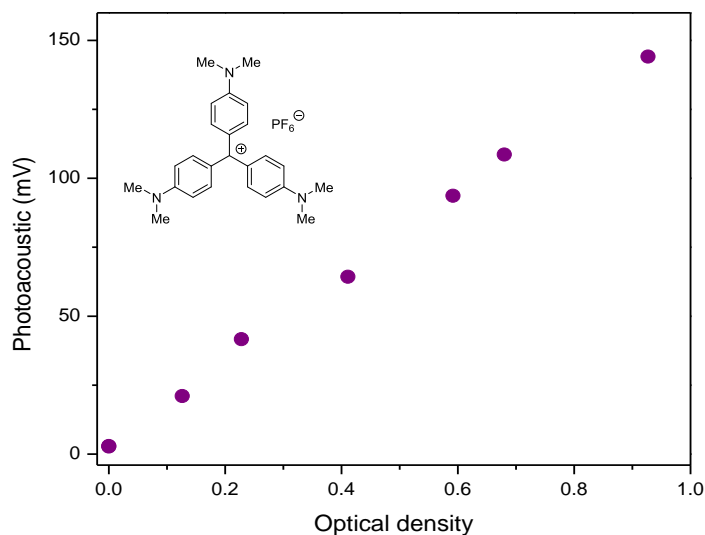

Figure S5. Photoacoustic response as a function of optical density for crystal violet in acetonitrile (laser fluence of 540 mJ cm^{-2}).
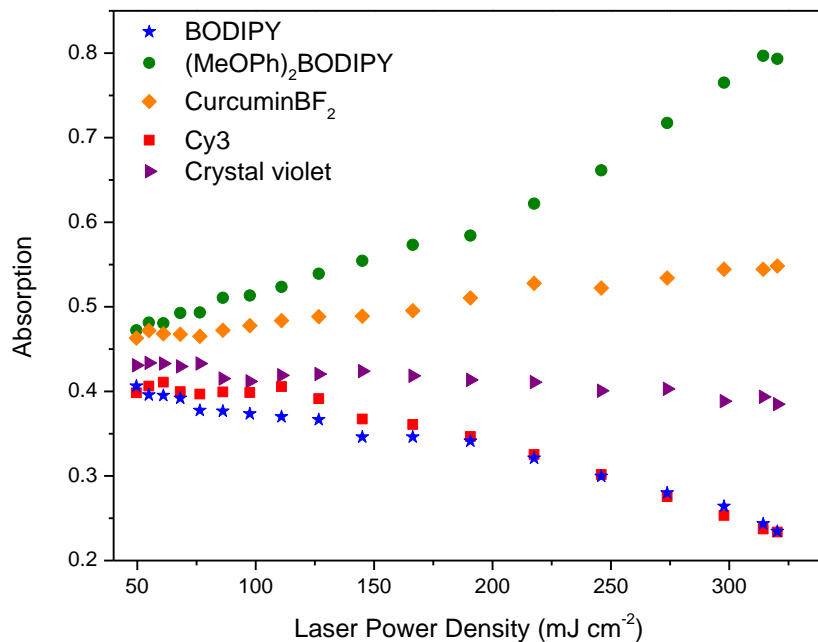
Figure S6. Optical absorption profiles of BODIPY, (MeOPh)2BODIPY, CurcuminBF2, Cy3 and Crystal violet with respect to laser fluence at λ_{exc} = 532 nm. Recorded by the optical Z-scan method as described above. All samples were prepared with an identical optical density of 0.3 in acetonitrile apart from (MeOPh)2BODIPY which was prepared in 9:1 v/v acetonitrile:dichloromethane. The corresponding PA data is plotted in Figure S7 below.

Figure S7. Photoacoustic emission profiles of BODIPY, (MeOPh)2BODIPY, CurcuminBF2, Cy3 and Crystal violet with respect to laser fluence at λ_{exc} = 532 nm. Recorded by the photoacoustic Z-scan method as described above. All samples were prepared with an identical optical density of 0.3 in acetonitrile apart from (MeOPh)2BODIPY which was prepared in 9:1 v/v acetonitrile:dichloromethane. The corresponding optical data is plotted in Figure S6 above.
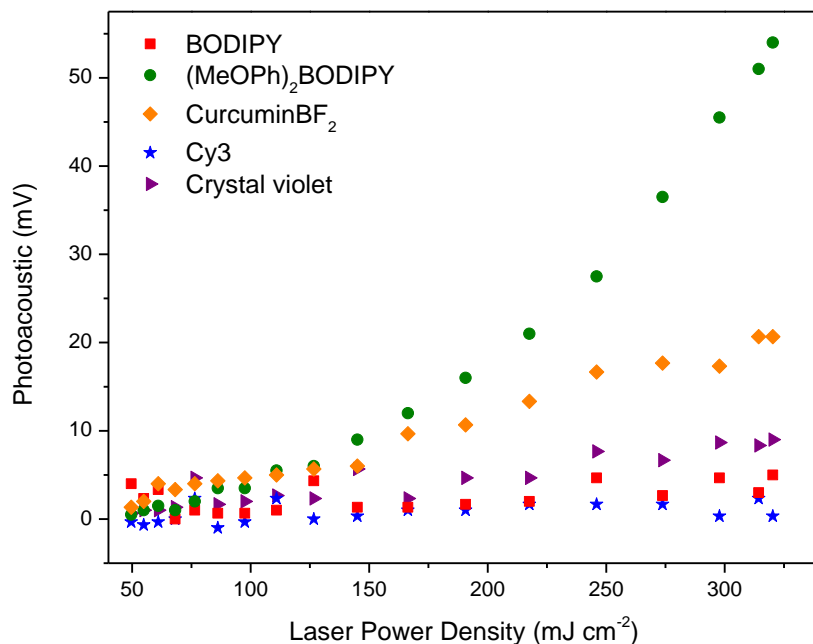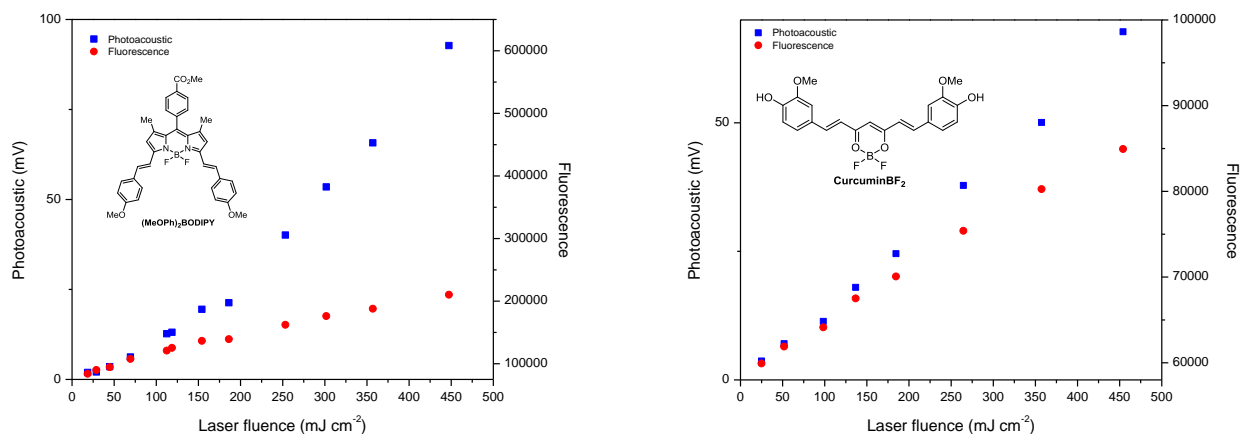
Figure S8. Photoacoustic and fluorescence emission from (MeOPh)$_2$BODIPY (left) and CurcuminBF$_2$ (right) as a function of laser fluence. At low laser fluence (< 50 mJ cm^{-2}) both the fluorescence and photoacoustic response increase in a concerted fashion with laser fluence as the concentration of S$_1$ excited states increases. At increased laser fluence (> 200 mJ cm^{-2}) S$_1 \rightarrow$S$_n$ excited state absorption gives rise to an enhanced S$_0 \leftarrow$S$_n$ photoacoustic signal with a correlated saturation S$_1$ states available for fluorescence decay.
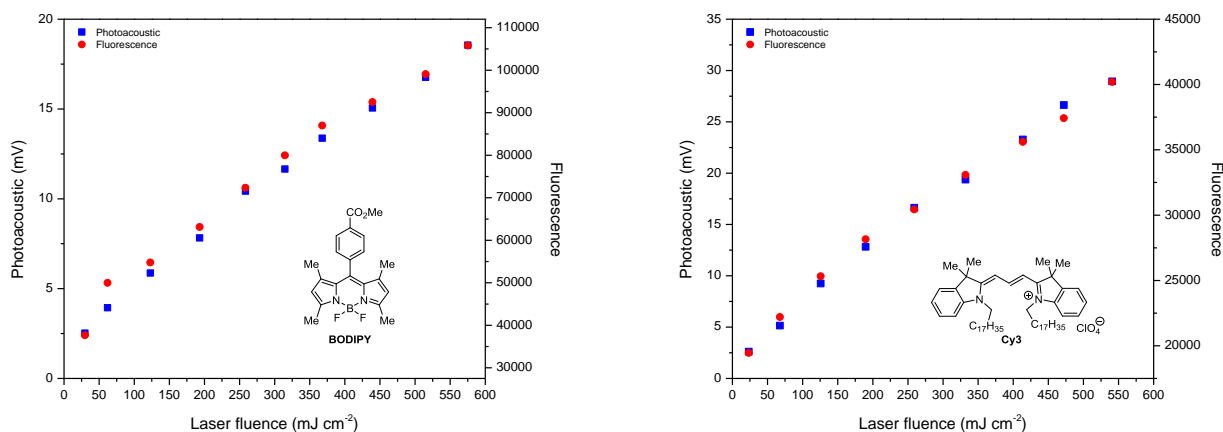
Figure S9. Correlated photoacoustic and fluorescence emission from BODIPY (left) and Cy3 (right) as a function of laser fluence. Both fluorescence and photoacoustic response increase in a concerted fashion with laser fluence as the concentration of S$_1$ excited states increases with laser fluence. Both dyes display ground state bleaching (Fig. S6) giving rise to a slight plateauing of the slope at high laser fluence.

S7

Figure S10. Quenching experiments for (MeOPh)$_2$BODIPY with and without 1.0 M 2,4-dinitrochlorobenzene (DNCB) sacrificial oxidant monitored by stead-state fluorescence (top-left), time-resolved fluorescence (top-right), optical Z-scan (bottom-left) and photoacoustic Z-scan (bottom-right).

Figure S11. Quenching experiments for curcuminBF$_2$ with and without 1.0 M 2,4-dinitrochlorobenzene (DNCB) sacrificial oxidant monitored by stead-state fluorescence (top-left), time-resolved fluorescence (top-right), optical Z-scan (bottom-left) and photoacoustic Z-scan (bottom-right).

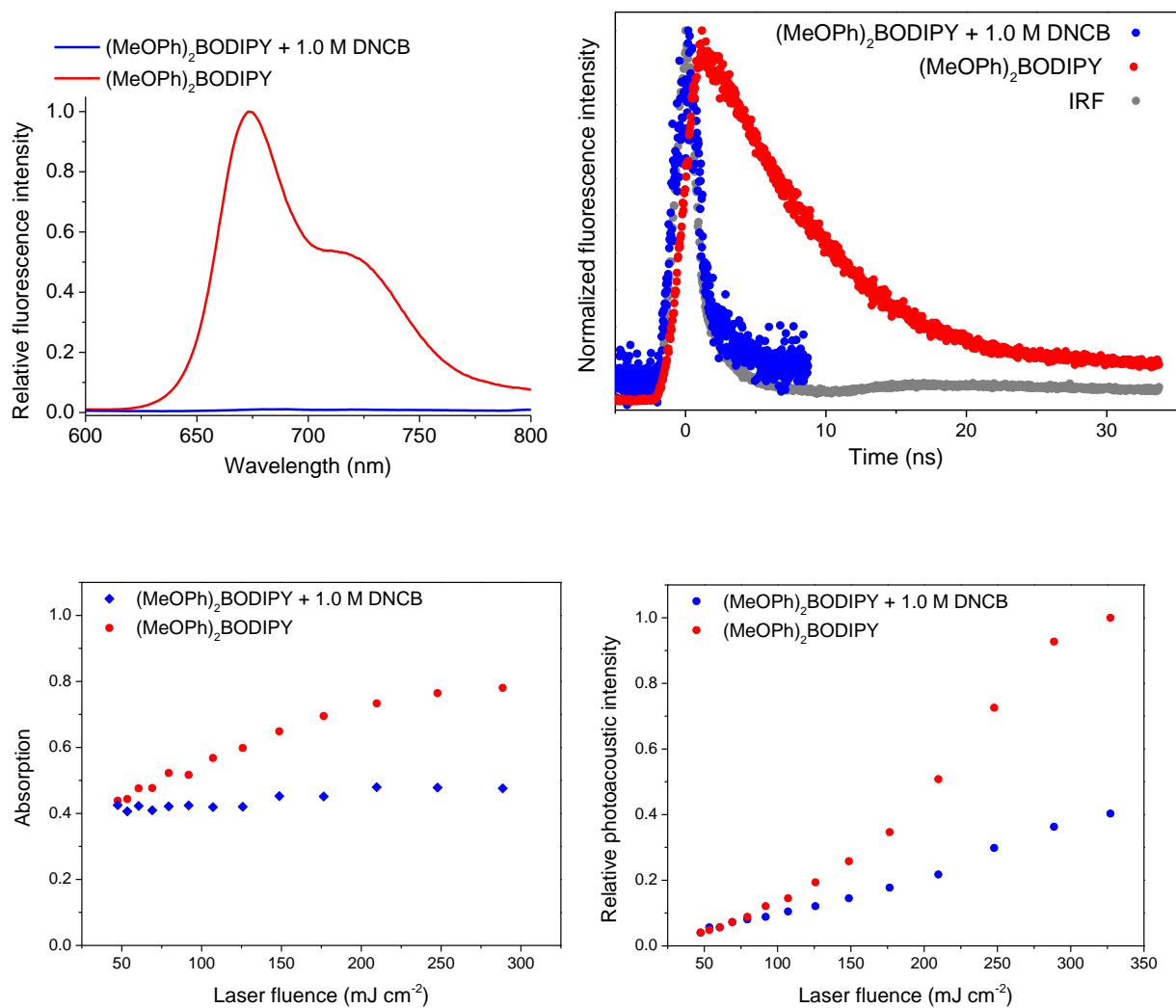**Figure S12.** Quenching experiments for BODIPY with and without 1.0 M 2,4-dinitrochlorobenzene (DNCB) sacrificial oxidant monitored by stead-state fluorescence (top-left), time-resolved fluorescence (top-right), optical Z-scan (bottom-left) and photoacoustic Z-scan (bottom-right).
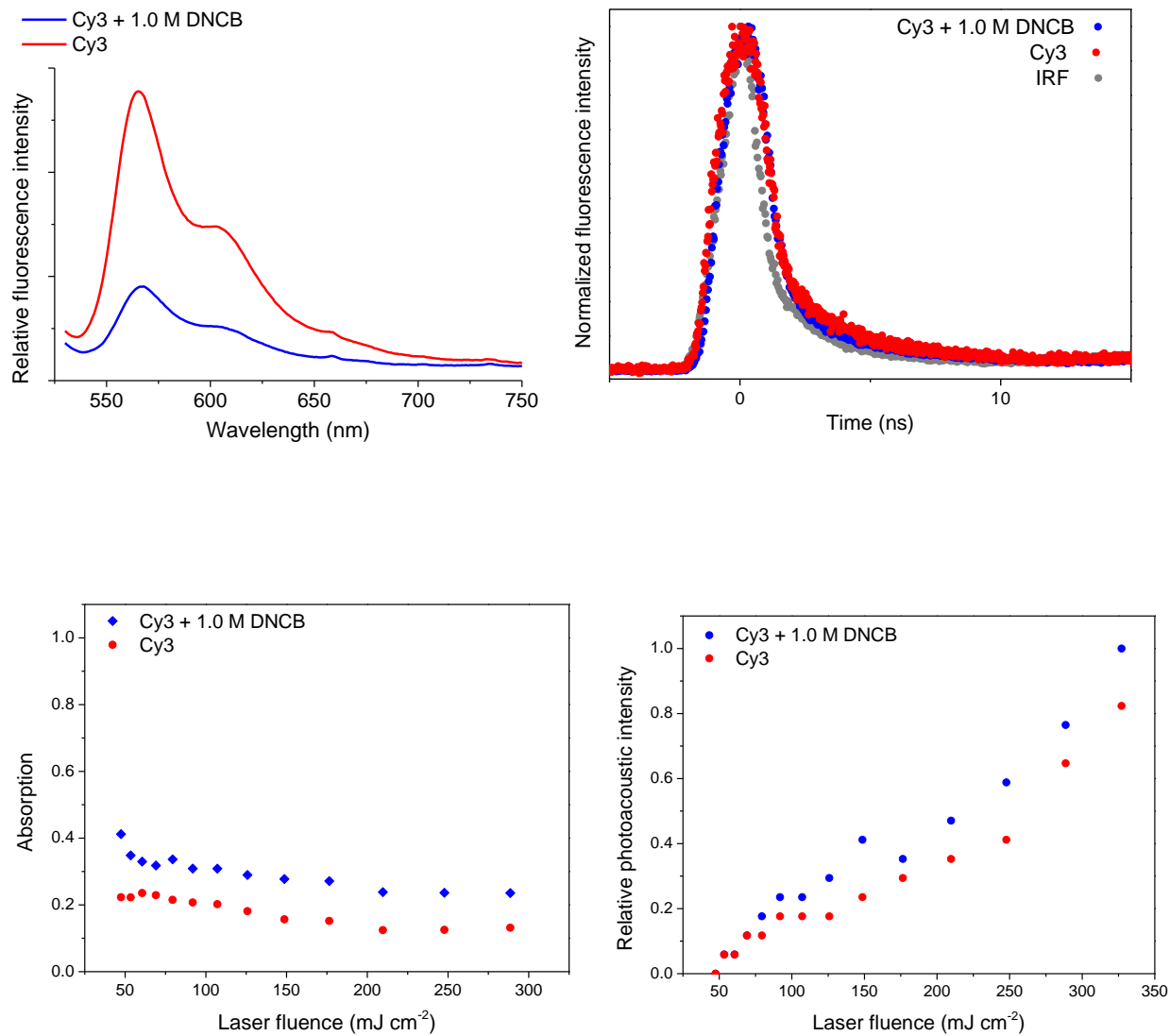
Figure S13. Quenching experiments for Cy3 with and without 1.0 M 2,4-dinitrochlorobenzene (DNCB) sacrificial oxidant monitored by stead-state fluorescence (top-left), time-resolved fluorescence (top-right), optical Z-scan (bottom-left) and photoacoustic Z-scan (bottom-right).
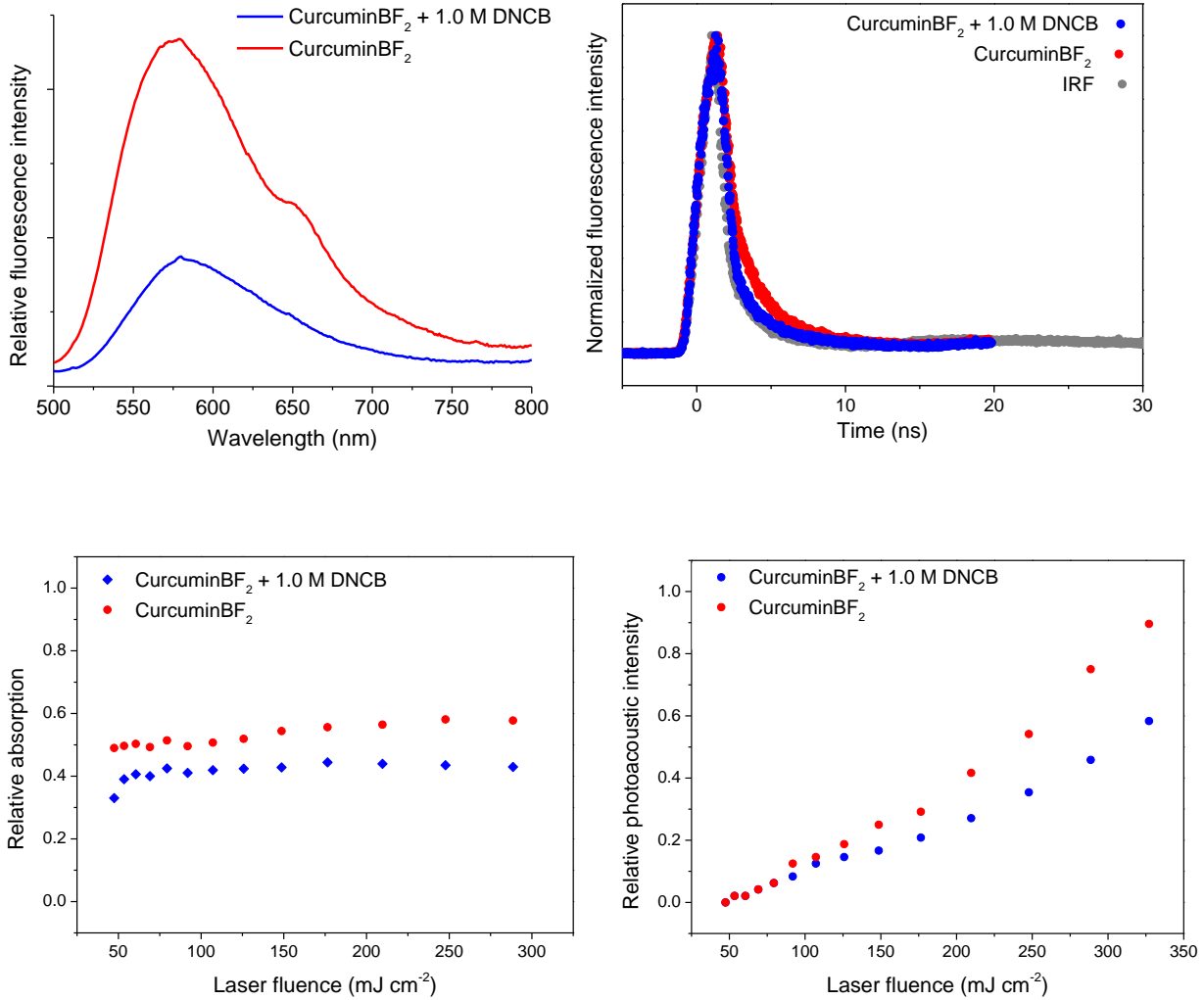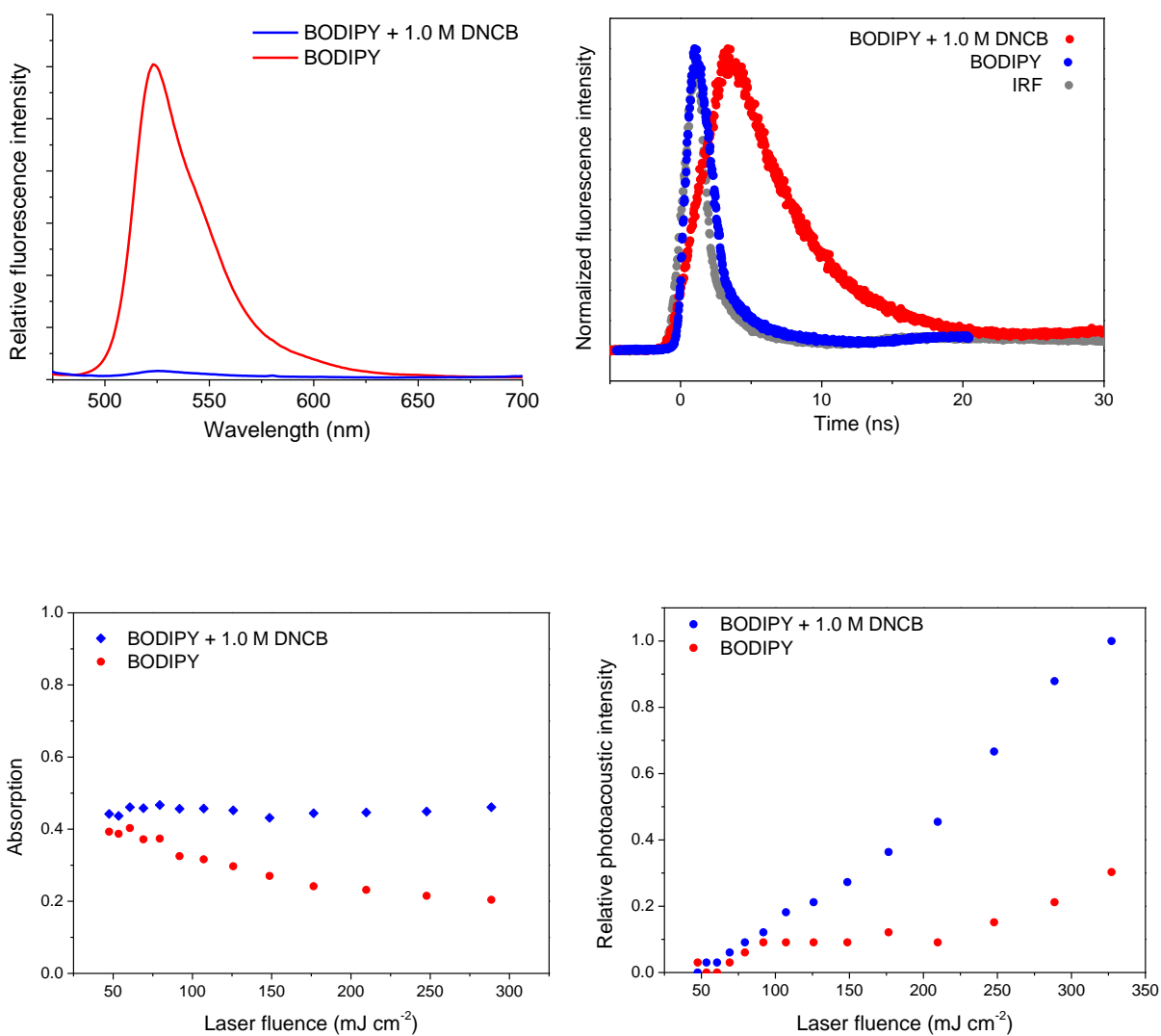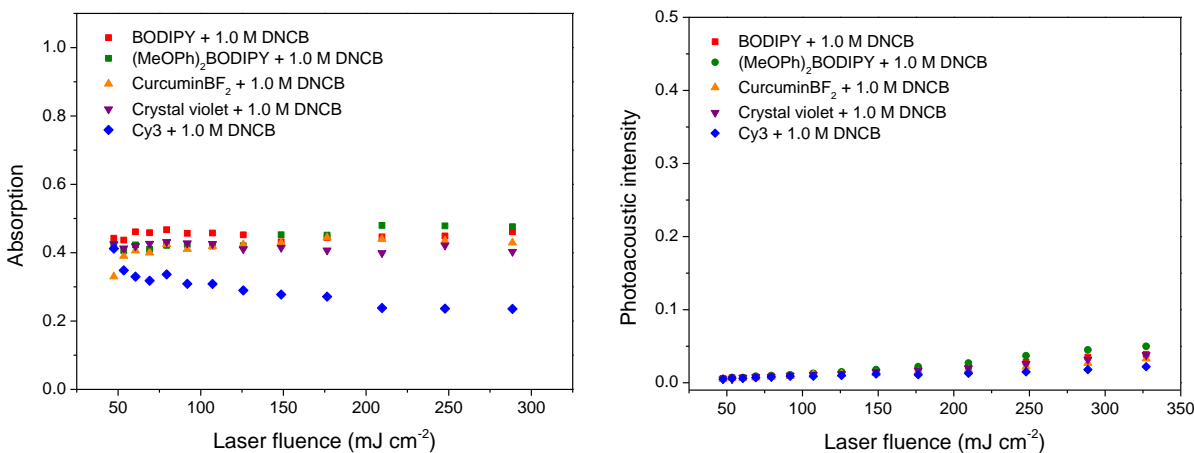
Figure S14. Overlay of quenching experiments all dyes with 1.0 M 2,4-dinitrochlorobenzene (DNCB) sacrificial oxidant monitored optical Z-scan (left) and photoacoustic Z-scan (right). Quenching of all dyes results in saturable absorber behavior similar to crystal violet with a short-lived excited state, negligible excited-state absorption and dramatically reduced photoacoustic signal.Cy3 still displays ground state bleaching in the optical Z-scan experiment as its excited state is already short lived resulting in inefficient quenching by DNCB.
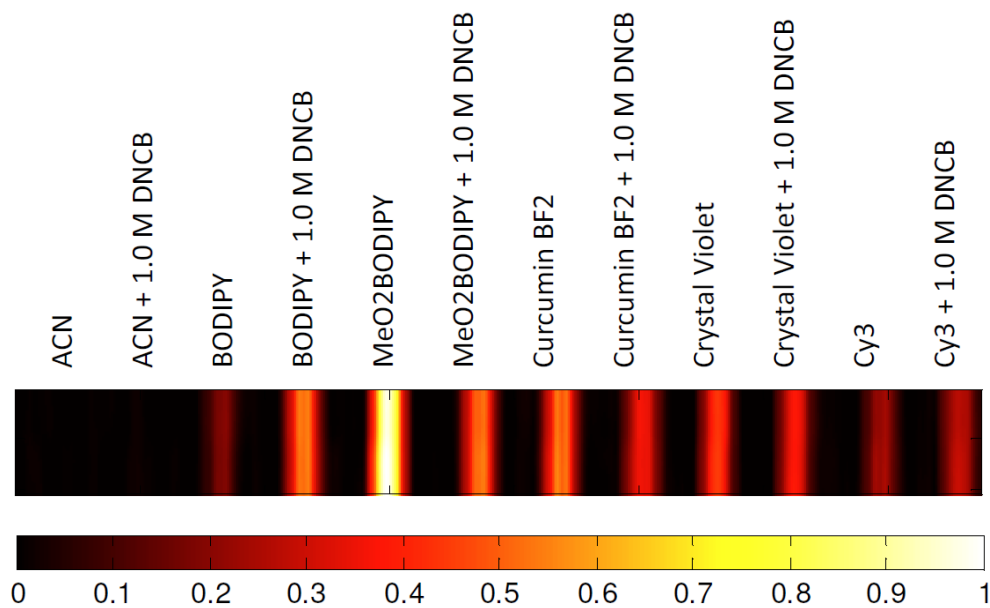
Figure S15. PAT image of all dyes with and without 1.0 M 2,4-dinitrochlorobenzene (DNCB) sacrificial oxidant recorded at a laser fluence of 366 mJ cm^{-2} (λ_{exc} = 532 nm; dimension = 26.40 mm x 6.65 mm). The color scale represents the normalized acoustic intensity.

Photoacoustic tomography (PAT) experimental details

A schematic of the PAT experimental setup is depicted in Scheme S2. The output of a frequency doubled Nd:YAG laser is directed onto a prism which allows the laser beam to focus on the sample at a 45^0 angle using a 10 cm confocal lens. The sample

is placed in a cell housing unit which is filled with water for acoustic signal coupling. A 10 MHz water immersion unfocused transducer (Olympus V311-SU) is placed directly above the sample. The sample is mounted on an automated XYZ translation stage (Thorlabs NRT 100) and moved along the x and y directions in discrete steps to perform a 2D raster scan. The PA signal is collected by the transducer and then amplified using a pulse amplifier that is fed to a Lecroy Wavepro oscilloscope for display and data collection. Sample scanning and data collection are both controlled by a Labview routine. By collecting data points along the XY plane a maximum intensity projection (MIP) is obtained by taking the absolute value of the Hilbert transform of the acquired signal via MATLAB. The MIP image is the map of optical absorption of the sample. The lateral resolution of the PAT system is dictated by the laser beam size which was estimated to be $70 \pm 5 \ \mu m$. Samples were prepared in spectroscopic grade acetonitrile using the same 2 mm path length cuvette as for PAZ sample preparation where a linear absorption coefficient (α) of 345 m^{-1} at the laser excitation wavelength 532 nm (optical density = 0.3) was chosen for consistency. Again, a 9:1 v/v acetonitrile:dichloromethane mixture was required for (MeOPh)2BODIPY alone to prevent precipitation during data collection. The dye solutions were loaded into 1 mm path length borosilicate tubes and then placed parallel in the Y direction at the bottom of the cell housing unit.
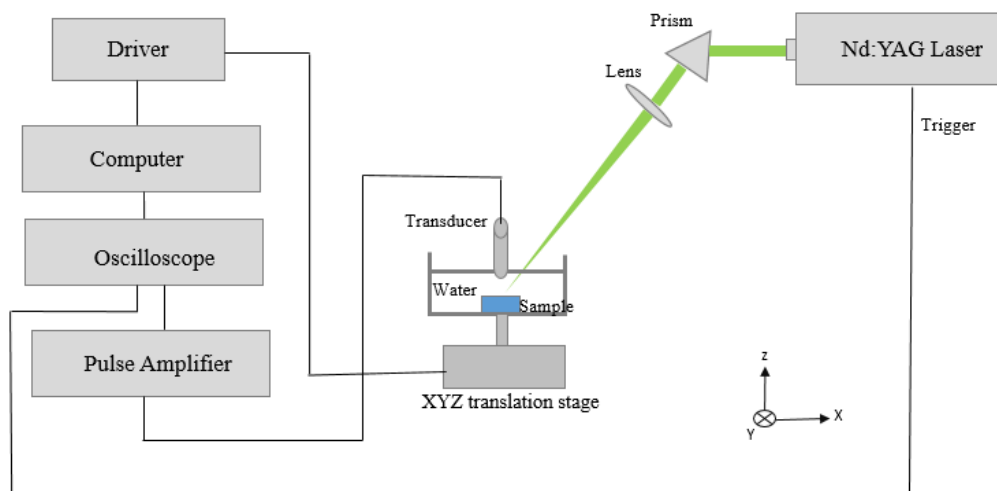
Scheme S2. Experimental setup of the photoacoustic tomography (PAT) apparatus.

(a) (b)   (c)   (d) (e)   (f)   (a) (b)   (c)   (d) (e)   (f)
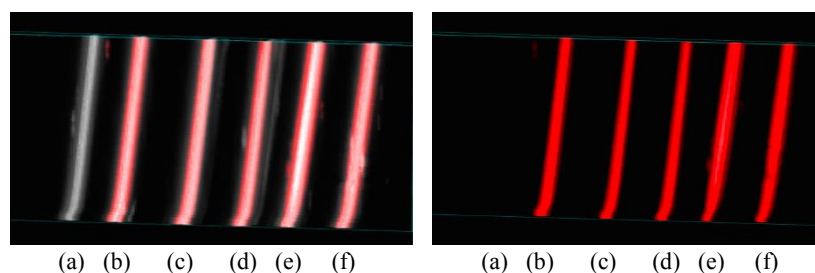
Figure S16. Photoacoustic tomography of dyes recorded in acetonitrile (optical density = 0.3) at a laser fluence of 20 mJ cm^{-2} (λ_{exc} = 532 nm) on a commercial Vevo LAZR Photoacoustics system. The left image includes a superposition of the ultrasound image showing the sample tube compartments whereas the right image includes the pure PA signal. Sample legend is (a) acetonitrile blank (b) BODIPY (v) (MeOPh)$_2$BODIPY (c) CurcuminBF$_2$ (d) Crystal violet (e) Cy3.

Table S2. Cartesian coordinates of geometry optimized structure for BODIPY.

		x	y	z
1	C	3.12109	2.503528	0.328872
2	C	2.003826	3.353749	0.210722
3	C	0.859934	2.572483	0.11626
4	H	2.044755	4.432989	0.197154
5	C	-0.52803	3.123408	-0.02092
6	H	-1.00936	2.801642	-0.94734
7	H	-1.17877	2.813743	0.800176
8	H	-0.48885	4.214449	-0.02411
9	C	1.305749	1.21053	0.177852
10	N	2.70052	1.225295	0.307531
11	C	0.612338	-0.00751	0.133297
12	C	1.286901	-1.2347	0.207367
13	C	0.819912	-2.5905	0.178014
14	N	2.681435	-1.26828	0.336722
15	C	1.951463	-3.38728	0.290131
16	C	3.082001	-2.55215	0.387908
17	C	-0.57701	-3.12212	0.056611
18	H	-1.06462	-2.79503	-0.86447
19	H	-1.21361	-2.80181	0.88488
20	H	-0.55343	-4.21361	0.055716
21	H	1.975084	-4.46705	0.302396
22	B	3.609619	-0.02726	0.434829
23	F	4.556053	-0.04588	-0.60179
24	F	4.26943	-0.0178	1.674456
25	C	-0.87677	0.003069	0.012642
26	C	-3.67186	0.02833	-0.20041
27	C	-1.67441	0.016171	1.162238
28	C	-1.49108	0.001379	-1.24354
29	C	-2.87786	0.013947	-1.35215
30	C	-3.05982	0.028831	1.057446
31	H	-1.20466	0.017222	2.139245
32	H	-3.34801	0.013127	-2.32658
33	H	-0.87841	-0.00949	-2.13804
34	H	-3.68428	0.039868	1.942429
35	C	-5.16272	0.044704	-0.25672
36	O	-5.8826	0.055693	0.715377
37	O	-5.63169	0.046489	-1.52258
38	C	4.509623	-2.9604	0.5283
39	C	4.554642	2.893316	0.461351
40	H	4.588246	-4.04779	0.549032

#		x	y	z
41	H	5.107482	-2.57402	-0.30085
42	H	4.940933	-2.55416	1.446929
43	H	5.148952	2.471941	-0.35317
44	H	4.976587	2.509651	1.393975
45	H	4.649927	3.979461	0.448609
46	C	-7.06445	0.062558	-1.66145
47	H	-7.48128	0.957276	-1.19721
48	H	-7.25143	0.062861	-2.73298
49	H	-7.50149	-0.82089	-1.19416

Table S3. Cartesian coordinates of geometry optimized structure for (MeOPh)$_2$BODIPY.

#		x	y	z
1	C	-0.17	-0.0499	2.541616
2	C	-1.31594	-0.06468	3.378353
3	C	-2.44513	-0.07988	2.583889
4	H	-1.30664	-0.06532	4.457509
5	C	-3.84778	-0.09827	3.115725
6	H	-4.42191	0.774314	2.795821
7	H	-4.40212	-0.98086	2.788866
8	H	-3.82338	-0.1023	4.207353
9	C	-1.98062	-0.07244	1.222151
10	N	-0.58734	-0.05382	1.249124
11	C	-2.67071	-0.08164	0.000024
12	C	-1.98051	-0.07247	-1.22205
13	C	-2.44502	-0.07992	-2.5838
14	N	-0.58718	-0.05396	-1.24897
15	C	-1.31583	-0.0648	-3.37825
16	C	-0.1699	-0.0501	-2.5415
17	C	-3.84766	-0.09824	-3.11566
18	H	-4.42175	0.774372	-2.79577
19	H	-4.40205	-0.98081	-2.78883
20	H	-3.82324	-0.10227	-4.20729
21	H	-1.30653	-0.06551	-4.4574
22	B	0.334469	-0.03373	-7.7E-05
23	F	1.127547	1.127678	-0.00015
24	F	1.17981	-1.15788	-0.00002
25	C	-4.16431	-0.10198	-1.2E-05
26	C	-6.97009	-0.13794	-3.7E-05
27	C	-4.85885	-1.31723	-5.9E-05
28	C	-4.88987	1.094037	0.000016
29	C	-6.28082	1.079777	0.000001
30	C	-6.24833	-1.33617	-7.1E-05

31	H	-4.30464	-2.24913	-7.9E-05
32	H	-6.83492	2.009217	0.000037
33	H	-4.35977	2.039834	0.00006
34	H	-6.79111	-2.27349	-9.7E-05
35	C	-8.45915	-0.21673	0.000008
36	O	-9.09035	-1.2489	0.00018
37	O	-9.04032	1.002314	-0.00011
38	C	1.222358	-0.03493	-2.90096
39	C	1.222269	-0.03451	2.901004
40	H	1.919568	-0.02568	-2.07384
41	H	1.919445	-0.0249	2.073859
42	C	1.678852	-0.0354	4.174742
43	H	0.9557	-0.04655	4.986574
44	C	3.070225	-0.02491	4.601245
45	C	5.738023	-0.01024	5.533834
46	C	3.369117	-0.03055	5.971705
47	C	4.160056	-0.01092	3.703086
48	C	5.46358	-0.00382	4.156575
49	C	4.6794	-0.02344	6.444721
50	O	7.055424	-0.00328	5.875965
51	C	7.402453	-0.00724	7.255218
52	H	7.031254	-0.90745	7.756634
53	H	7.017068	0.881803	7.765854
54	H	8.490542	0.001428	7.28726
55	H	4.858871	-0.02878	7.511301
56	H	2.555209	-0.04124	6.689763
57	H	6.296674	0.006397	3.463908
58	C	1.678905	-0.03559	-4.17471
59	H	0.95573	-0.04626	-4.98652
60	C	3.070269	-0.02538	-4.60124
61	C	5.738051	-0.01098	-5.53387
62	C	4.160126	-0.01268	-3.70309
63	C	3.369126	-0.02996	-5.9717
64	C	4.679402	-0.02295	-6.44475
65	C	5.463642	-0.00572	-4.1566
66	O	7.055447	-0.00423	-5.87603
67	C	7.402442	-0.00703	-7.25529
68	H	2.555199	-0.0397	-6.68975
69	H	4.858846	-0.02741	-7.51133
70	H	3.981075	-0.00877	-2.63478
71	H	3.980973	-0.00605	2.634785
72	H	6.296755	0.0035	-3.46395
73	H	8.490533	0.001261	-7.28735

74	H	7.030893	-0.90663	-7.75754
75	H	7.017379	0.882636	-7.76509
76	C	-10.4796	1.012181	-4.3E-05
77	H	-10.8636	0.510092	0.888912
78	H	-10.7621	2.062643	-6.2E-05
79	H	-10.8637	0.510015	-0.88893

Table S4. Cartesian coordinates of geometry optimized structure for CurcuminBF$_2$.

1	C	1.208992	0.91285	-0.06945
2	C	0.000469	0.208904	-0.13219
3	C	-1.20844	0.912659	-0.0757
4	O	-1.23226	2.214388	-0.04946
5	C	2.478319	0.213288	-0.0023
6	C	-2.47784	0.212887	-0.01068
7	C	-3.65933	0.871056	0.054717
8	C	3.659915	0.871412	0.061072
9	C	-4.99375	0.300069	0.131565
10	C	-7.62692	-0.70718	0.299818
11	C	-5.24505	-1.0881	0.135036
12	C	-6.0987	1.166845	0.199255
13	C	-7.39525	0.670117	0.281223
14	C	-6.53174	-1.59873	0.214657
15	C	4.994409	0.300113	0.13472
16	C	7.62731	-0.70813	0.297617
17	C	5.244892	-1.08819	0.138114
18	C	6.099905	1.166465	0.19874
19	C	7.396473	0.669259	0.277622
20	C	6.531537	-1.59921	0.215415
21	O	1.232372	2.214544	-0.04036
22	B	0.000906	3.059735	-0.29185
23	F	0.006426	3.451823	-1.6059
24	F	-0.00307	4.08968	0.602436
25	H	-3.60886	1.958134	0.051579
26	H	-2.42443	-0.872	-0.01329
27	H	0.00052	-0.87348	-0.14861
28	H	2.424777	-0.8716	-0.00419
29	H	3.60984	1.958495	0.057704
30	H	5.937495	2.240706	0.191568
31	H	8.241329	1.353136	0.337057
32	H	4.432393	-1.80566	0.089404
33	H	-5.93623	2.241024	0.192126
34	H	-8.23951	1.354466	0.343912

		x	y	z
35	H	-4.43299	-1.80595	0.084316
36	O	-8.87379	-1.24659	0.407956
37	O	-6.70018	-2.9571	0.285145
38	O	8.874028	-1.24802	0.404827
39	O	6.700153	-2.95756	0.287078
40	H	-9.52322	-0.52857	0.473406
41	H	9.523736	-0.53023	0.469761
42	C	-7.4037	-3.56644	-0.80296
43	C	7.396065	-3.56844	-0.80498
44	H	-8.44592	-3.23669	-0.84415
45	H	-6.90815	-3.34642	-1.75762
46	H	-7.36648	-4.64172	-0.61595
47	H	7.373403	-4.64242	-0.60848
48	H	6.885522	-3.36197	-1.75481
49	H	8.433999	-3.22783	-0.86268

Table S5. Cartesian coordinates of geometry optimized structure for Crystal violet.

		x	y	z
1	C	2.190732	-1.01222	-0.65513
2	C	3.566034	1.010903	0.673203
3	C	1.443271	0	-4.1E-05
4	C	3.566041	-1.01092	-0.67324
5	C	4.308935	-2.5E-05	0.000007
6	C	2.190726	1.012217	0.655055
7	C	0	0	-4.5E-05
8	C	-0.72164	-1.24991	-4.1E-05
9	C	-2.15449	-3.73164	0.000007
10	C	-0.21876	-2.40333	0.655055
11	C	-1.97197	-1.39112	-0.65513
12	C	-2.65851	-2.58282	-0.67324
13	C	-0.90755	-3.59373	0.673203
14	C	-0.72164	1.249909	-4.1E-05
15	C	-2.15445	3.731659	0.000007
16	C	-1.97197	1.391116	0.655055
17	C	-0.21876	2.403339	-0.65513
18	C	-0.90754	3.593744	-0.67324
19	C	-2.65849	2.582825	0.673203
20	N	-2.83405	-4.90863	0.000052
21	N	5.668025	-4.1E-05	0.000052
22	N	-2.83398	4.908674	0.000052
23	C	-4.14645	5.011015	0.636184
24	C	-2.26644	6.09648	-0.63611

		x	y	z
25	C	6.412889	1.08542	0.636184
26	C	6.412924	-1.08545	-0.63611
27	C	-2.26644	-6.09644	0.636184
28	C	-4.14649	-5.01103	-0.63611
29	H	-4.56293	-5.99445	-0.4319
30	H	-4.83757	-4.26245	-0.23863
31	H	-4.07996	-4.88686	-1.72236
32	H	-2.91004	-6.94876	0.432284
33	H	-2.19186	-5.97661	1.722398
34	H	-1.27274	-6.32079	0.238448
35	H	-0.49579	-4.42355	1.229539
36	H	-3.58303	-2.64115	-1.22958
37	H	-2.37519	-0.55056	-1.20633
38	H	0.710818	-2.33225	1.206226
39	H	1.664392	-1.7817	-1.20633
40	H	4.078814	-1.78242	-1.22958
41	H	4.078804	1.782406	1.229539
42	H	1.664381	1.781713	1.206226
43	H	0.7108	2.332255	-1.20633
44	H	7.472813	-0.95438	-0.4319
45	H	6.110173	-2.05824	-0.23863
46	H	6.272125	-1.08992	-1.72236
47	H	7.472823	0.954214	0.432284
48	H	6.271824	1.090092	1.722398
49	H	6.110335	2.058166	0.238448
50	H	-0.49579	4.423567	-1.22958
51	H	-2.3752	0.55054	1.206226
52	H	-3.58301	2.641145	1.229539
53	H	-4.83759	4.262622	0.238448
54	H	-4.07996	4.886512	1.722398
55	H	-4.56279	5.994547	0.432284
56	H	-2.90989	6.948838	-0.4319
57	H	-1.2726	6.320684	-0.23863
58	H	-2.19217	5.976778	-1.72236

Table S6. Cartesian coordinates of geometry optimized structure for Cy3.

		x	y	z
1	C	5.309714	0.000000	2.040153
2	C	6.265186	0.000000	-0.621245
3	C	4.445522	0.000000	0.952044
4	C	6.680145	0.000000	1.768386
5	C	7.155488	0.000000	0.45723

6	C	4.903408	0.000000	-0.363683
7	N	3.022054	0.000000	0.942189
8	C	2.539685	0.000000	-0.318535
9	C	3.717473	0.000000	-1.304856
10	C	-5.30971	0.000000	2.040153
11	C	-6.26519	0.000000	-0.621245
12	C	-4.44552	0.000000	0.952044
13	C	-6.68015	0.000000	1.768386
14	C	-7.15549	0.000000	0.45723
15	C	-4.90341	0.000000	-0.363683
16	N	-3.02205	0.000000	0.942189
17	C	-2.53969	0.000000	-0.318535
18	C	-3.71747	0.000000	-1.304856
19	C	1.219396	0.000000	-0.772546
20	C	0.000000	0.000000	-0.089156
21	C	-1.2194	0.000000	-0.772546
22	C	3.696799	-1.271312	-2.185698
23	C	3.696799	1.271312	-2.185698
24	C	-3.6968	-1.271312	-2.185698
25	C	-3.6968	1.271312	-2.185698
26	C	2.227439	0.000000	2.161329
27	C	-2.22744	0.000000	2.161329
28	H	-4.96084	0.000000	3.065106
29	H	-7.38157	0.000000	2.594016
30	H	-8.22295	0.000000	0.273667
31	H	-6.64134	0.000000	-1.638256
32	H	-3.70338	-2.177417	-1.576545
33	H	-2.81523	-1.292757	-2.830116
34	H	-4.58159	-1.286718	-2.825672
35	H	-4.58159	1.286718	-2.825672
36	H	-2.81523	1.292757	-2.830116
37	H	1.143387	0.000000	-1.854584
38	H	-1.14339	0.000000	-1.854584
39	H	0.000000	0.000000	0.988892
40	H	1.602482	0.894644	2.209813
41	H	1.602482	-0.894644	2.209813
42	H	2.890475	0.000000	3.021509
43	H	-1.60248	0.894644	2.209813
44	H	-1.60248	-0.894644	2.209813
45	H	-2.89048	0.000000	3.021509
46	H	7.381574	0.000000	2.594016
47	H	4.960838	0.000000	3.065106
48	H	8.222953	0.000000	0.273667

49	H	6.64134	0.000000	-1.638256
50	H	4.581592	-1.286718	-2.825672
51	H	3.70338	-2.177417	-1.576545
52	H	2.815232	-1.292757	-2.830116
53	H	2.815232	1.292757	-2.830116
54	H	3.70338	2.177417	-1.576545
55	H	4.581592	1.286718	-2.825672
56	H	-3.70338	2.177417	-1.576545

References

1. Ikawa, Y.; Moriyama, S.; Furuta, H., *Analytical Biochemistry* **2008,** *378*, 166-170.
2. Hong, X.; Wang, Z.; Yang, J.; Zheng, Q.; Zong, S.; Sheng, Y.; Zhu, D.; Tang, C.; Cui, Y., *Analyst* **2012,** *137*, 4140-4149.
3. Liu, K.; Chen, J.; Chojnacki, J.; Zhang, S., *Tetrahedron Lett.* **2013,** *54*, 2070-2073.
4. Magde, D.; Wong, R.; Seybold, P. G., *Photochemistry and Photobiology* **2002,** *75*, 327-334.
5. Fischer, M.; Georges, J., *Chemical Physics Letters* **1996,** *260*, 115-118.
6. Harihara.Pc; Pople, J. A., *Theoretica Chimica Acta* **1973,** *28*, 213-222.
7. Francl, M. M.; Pietro, W. J.; Hehre, W. J.; Binkley, J. S.; Gordon, M. S.; Defrees, D. J.; Pople, J. A., *J. Chem. Phys.* **1982,** *77*, 3654-3665.
8. Tomasi, J.; Mennucci, B.; Cammi, R., *Chem. Rev.* **2005,** *105*, 2999-3093.
9. Scalmani, G.; Frisch, M. J.; Mennucci, B.; Tomasi, J.; Cammi, R.; Barone, V., *J. Chem. Phys.* **2006,** *124*, 94107.